



Article

A Study of Raindrop Impacts on a Wind Turbine Material: Velocity and Impact Angle Effects on Erosion MAPS at Various Exposure Times

Samuel Groucott , Kieran Pugh *D, Iasonas Zekos and Margaret M Stack D

Tribology Laboratory, Department of Mechanical Engineering, University of Strathclyde Glasgow, 16 Richmond St., Glasgow G1 1XQ, UK; samuel.groucott.2016@uni.strath.ac.uk (S.G.); iasonas.zekos@strath.ac.uk (I.Z.); margaret.stack@strath.ac.uk (M.M.S.)

* Correspondence: kieran.pugh@strath.ac.uk; Tel.: +44-0775-711-2735

Abstract: Within renewable energy, challenging climates can impose great limitations on power generation. In wind energy, rain erosion on turbine blades can create major disruptions to air flow over the aerofoil, reducing the efficiency of the blade and immediately affecting the power output of the turbine. The defects in the materials that cause these inefficiencies are known and can be observed on turbines that have been in operation for extended periods. This work explores the transitions between different wear states for G10 Epoxy Glass under laboratory simulated wind turbine conditions in operation and measures the wear periodically to identify a progression of erosion. Mass loss data and micrographic analysis revealed samples at 45° and 60° displayed increasing erosion when examining erosion performance for angles between 15° and 90° over various exposure and velocities. Erosion maps were constructed, showing the variation of wastage and identifying the performance window of conditions where degradation is minimised.

Keywords: composites; erosion; energy; maps; wind; turbine



Citation: Groucott, S.; Pugh, K.; Zekos, I.; M Stack, M. A Study of Raindrop Impacts on a Wind Turbine Material: Velocity and Impact Angle Effects on Erosion MAPS at Various Exposure Times. *Lubricants* **2021**, *9*, 60. https://doi.org/10.3390/ lubricants9060060

Received: 4 March 2021 Accepted: 27 May 2021 Published: 3 June 2021

Publisher's Note: MDPI stays neutral with regard to jurisdictional claims in published maps and institutional affiliations.



Copyright: © 2021 by the authors. Licensee MDPI, Basel, Switzerland. This article is an open access article distributed under the terms and conditions of the Creative Commons Attribution (CC BY) license (https://creativecommons.org/licenses/by/4.0/).

1. Introduction

Renewable energy is now at the forefront of energy production with wind increasingly becoming the most popular generation mode. With these developments in wind energy, the technology behind capturing energy from wind has been evolving and has produced turbines that can generate up to 12 MW [1]. In order to generate significant magnitudes of energy, the turbine must have a large swept area which results in the glass fibre reinforced polymer blades being up to 100 m long each. When blades of this size are in operation, the tips can be travelling up to 300 mph. At these speeds, any material is vulnerable to impacts, which is why rain droplets can easily damage blades when in operation. The damage created will affect the aerodynamic properties of the blade and hence the power output of the turbine [2]. Despite this issue, wind energy has continued to grow.

With the potential of wind power to become a global source of renewable energy, both on and offshore wind have seen significant growth since the 1990s across the world. By 2008, there was a global installed capacity of 100 GW, with wind producing 4% of global energy generation by 2016. In a decade, global capacity grew over 5.5 times to 564 GW by 2018 and provided 1.2 million jobs in the wind power sector. In the same year, wind energy saw a near USD 29.4 billion investment from the European Union, translating to USD 1.54 million and USD 9.57 million per onshore and offshore MW installations, respectively [3].

This accelerated sector growth is due to increased turbine size [4], allowing for greater energy generation and efficiency, reducing the ratio of installation to production cost for wind farms. This change increases the potential capacities for new turbines and creates new areas of low wind which were previously inaccessible with smaller turbines [3]. Between 2018 and 2025, onshore and off-shore wind turbine blade rotor diameters are predicted to increase 154% and 155%, respectively.

Lubricants **2021**, 9, 60 2 of 12

The first point of contact of flow on a turbine blade is its leading edge, making it the most vulnerable point of damage from the environment. This point guides the wind flow over and under the blade's edge, creating the surface pressure difference which causes the lift force, driving the turbine. To create these pressure forces, blade surfaces must be smooth to produce less-turbulent flow. However, with the increase in leading edge roughness, the surface boundary layer grows and causes the steady turbulent flow to transition closer to the blade edge, which increases drag [5]. This increase has been studied by Sareen et al. [2], who concluded that after a relatively small amount of leading-edge erosion, drag was increased by 80%, resulting in approximately a 5% loss in annual energy production. Extending this to significant erosion and an increase of 400–500% in drag, the annual energy output could decrease by 25%. When energy production from wind is expected to reach 1000 GW, a 25% loss equating to 250 GW is monumental.

Degradation, and resulting roughness, are both caused primarily by exposure to environmental elements, including rain and hail [6], gradually wearing down the leading-edge surface. Wear begins in areas of material defects, where pinholes are formed. These lead to gouges which grow to cracks on the blade surface [7] as seen in Figure 1.

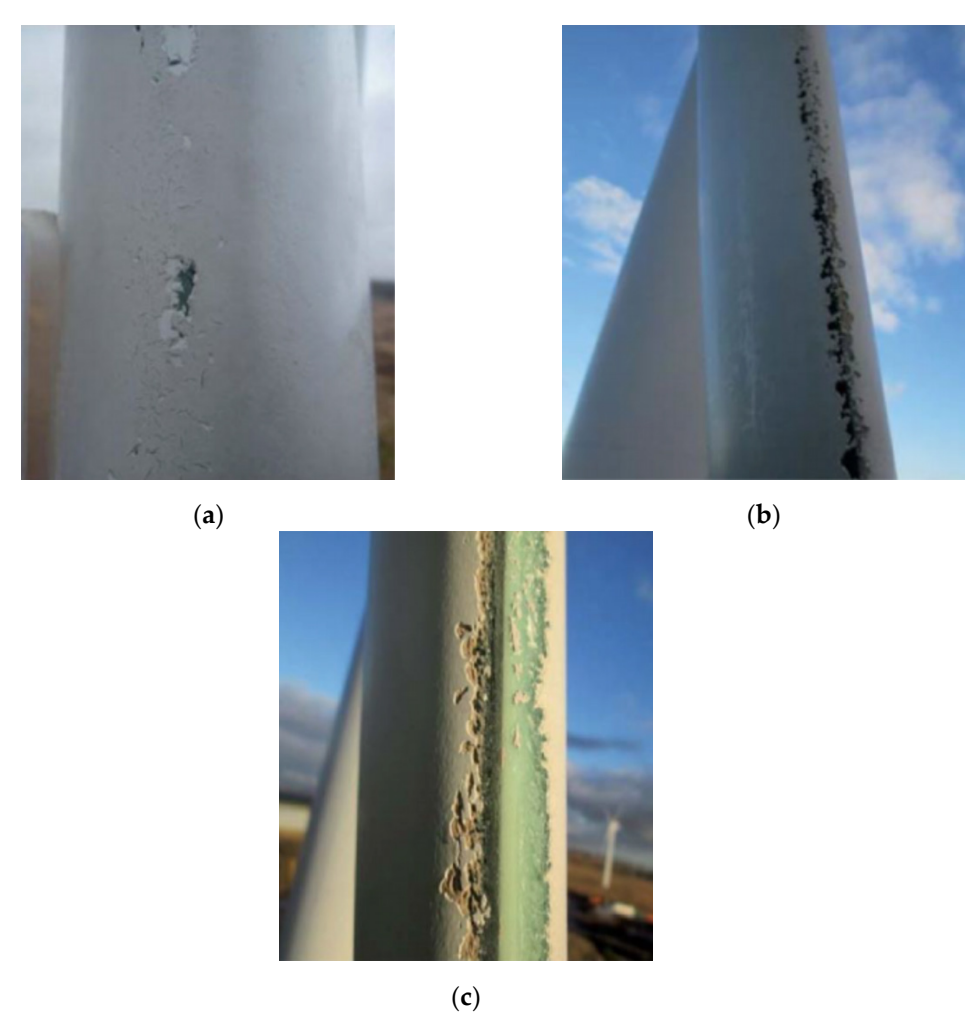


Figure 1. Damaged wind turbine blade at the leading-edge showing (**a**) pinholes, (**b**) gouges and removal of material, (**c**) major loss of material and damage to GFRP. Source: [8].

To evaluate these stages of erosion within a laboratory environment, the exposure experiment was carried out in cycles as the mass loss and damage needed to be inspected throughout the experiment, in order to identify the severity of damage. This information not only shows a wear rate of the material but also provides for future prediction estimates of erosion rates. In the wind energy sector, this information would be the most valuable,

Lubricants **2021**, 9, 60 3 of 12

allowing wind turbine owners to anticipate when the turbine blade will need maintenance to optimise energy production. Studies have investigated this in single exposure cycles [9]; however, this study analyses the erosion effects as a function of various impact angles over time, as well as the standard erosion rates. This is accomplished by running multiple samples at desired impact angles under an identical erosive environment. This will demonstrate the different erosion mechanisms that occur at different impact angles and how the erosion patterns on the sample will evolve over time.

2. Materials and Methods

2.1. Materials

G10 Epoxy Glass Fibre, consisting of carbon-based epoxy and silicate oxide fibres orientated in a 90-degree cross-weave, was the chosen sample material. Glass Fibre Reinforced Polymer (GFRP) is a common material in a turbine blade structure ref as it combines the structural rigidity needed to build large structures with the lightweight capabilities of complex geometries. The samples used were coupons with dimensions of 30×30 mm and 1 mm thickness. Samples were marked to ensure they were exposed at the same orientation, given the directional nature of the fibres in the material and their effect on mechanical properties. The samples required a drying period after testing due to the absorptive nature of the polymer material, as this would also significantly alter later mass measurements due to their moisture content. The chosen material was from the same batch as Rasool et al. [10], and the properties of the material are shown in Table 1.

Table 1. G10 Epoxy Glass laminate properties [10].

Property	Value
Flexural Strength (MPa)	482
Tensile Strength (MPa)	320
Shear Strength (MPa)	131
Impact (Notched Charpy) $(kJ m^{-2})$ Density $(g cm^{-3})$	65
Density (g cm ⁻³)	2
Specific Gravity	1.82
Water Absorption (mg m^{-2})	8
Rockwell Hardness (M-Scale)	110
Standard Finish	Satin/Glossy

2.2. Testing Conditions

The primary variables chosen for this investigation were the impact angle and impact velocity. The first was chosen to represent the different angles at which rain impacts on the turbine blade leading edge, helping to indicate the erosion wear mechanism taking place on the sample. The impact velocity represents different rotor velocities along the turbine blade, which is maximum at the blade tip. This helps indicate the level of erosion with a change in velocity and how it affects the rate of wear. The impact angles of the leading edge of the blade are demonstrated in Figure 2. All samples had the same test repeated in four identical cycles to produce continued, gradual wear to try and associate the exposure time of the samples to the development of defects such as pin holes, gouges and cracks [8].

Lubricants **2021**, 9, 60 4 of 12

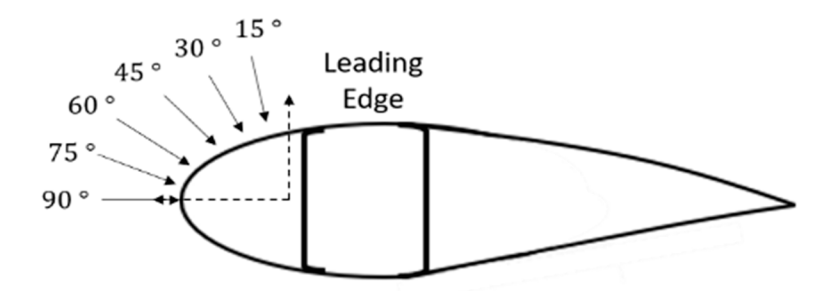


Figure 2. Test sample impact angle simulated to that of a point on a wind turbine leading edge.

To improve accuracy during each experiment, parameters were kept constant and a consistent methodology was followed. Common tap water was chosen as the best replacement for rainwater available and was taken from the same laboratory source. All experiments were performed using the same testing apparatus. The temperature inside the rig was monitored and maintained at 20 \pm 1 $^{\circ}\text{C}$.

2.3. Testing Apparatus

There are many ways to recreate the conditions of a wind turbine blade in the field within laboratory conditions and there have been some issues with cross referencing results from different methodologies [4,11,12]; however, the technique that replicates the conditions closest would be a whirling arm erosion rig (WARER) as stated by the DNVGL recommended practice [13]. The rig that was used for this investigation was built in the University of Strathclyde in the tribology laboratory to artificially simulate turbine blade conditions [14,15]. This was achieved with a water tank connected to the peristaltic pump through tubing, then connected to 16 droplet needles of the chosen gauge (23 G). These needles were tested to measure the average size of droplet they produce which was 2.40 mm; this was accomplished using high-speed photography. The droplets were also captured by the high-speed camera while the rig was in operation to determine there was little effect of aerodynamic forces. The needles were arranged as shown in Figure 3, inside a stainless-steel enclosure. Two samples of different impact angles were secured in the sample holders at each end of the removable rotor arm and adjusted to the desired angle orientation. The rotor arm was then secured in the test rig by a central hub, connecting it to the driving motor. The pump reservoir tank was then filled appropriately. Before testing, the pump was switched on and left to run for 5 min to ensure flow equilibrium and that all droplet needles were active.

A Perspex lid was then placed to enclose the test apparatus and the motor frequency was set for the corresponding impact velocity. A stopwatch was started once the motor reached the desired velocity, then stopped at the required experimental time. The motor and the rain-field were then stopped concurrently. The lid was removed once the arm came to a complete stop and samples were removed and left to dry in the tribology laboratory for at least 24 h.

The variable ranges were $15^{\circ}-90^{\circ}$ and $40~\mathrm{ms^{-1}}-60~\mathrm{ms^{-1}}$ for the impact angle and velocity, respectively, at increments of 15° and $10~\mathrm{ms^{-1}}$. Each experiment ran the same total distance of 216 km with tests running for 90, 72 and 60 min for $40~\mathrm{ms^{-1}}$, $50~\mathrm{ms^{-1}}$ and $60~\mathrm{ms^{-1}}$, respectively. Four repeated cycles were conducted in order to analyse the erosion periodically and produce stages of gradual erosion.

Lubricants **2021**, 9, 60 5 of 12

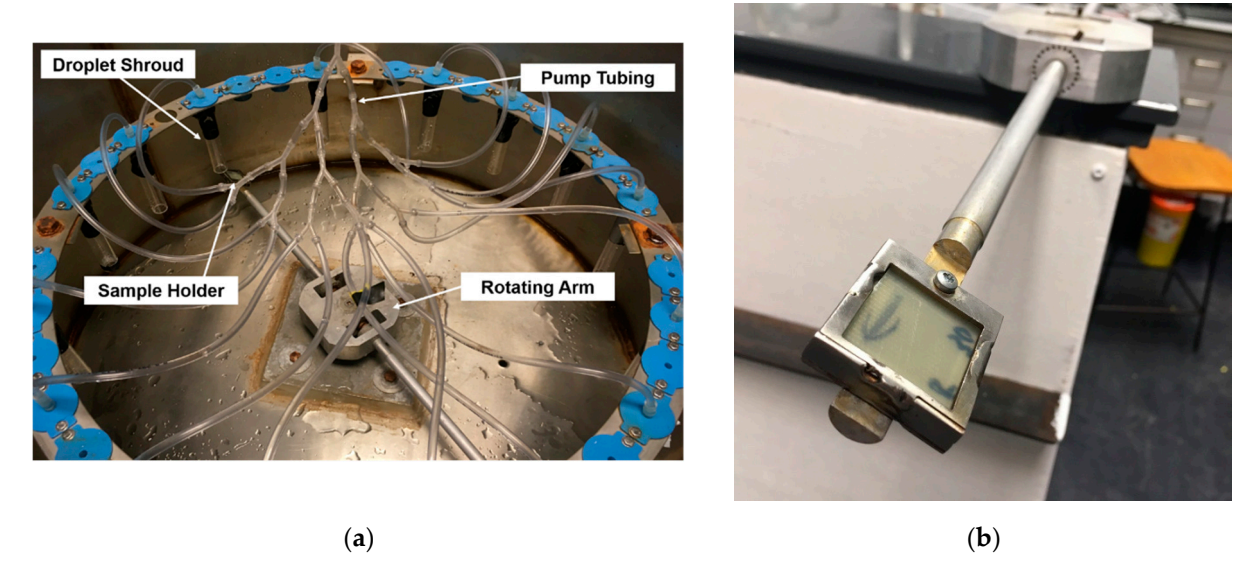


Figure 3. (a) Whirling arm rain erosion rig in the tribology lab within Strathclyde University (b) GFRP sample in holder.

2.4. Experimental Run Time

Samples were tested for the longest possible time to maximize exposure and the amount of erosion, while maintaining safe laboratory conditions in the WARER. The highest safe operation velocity of the rig was deemed to be $60~\rm ms^{-1}$. Although this is not the blade tip speed of $134~\rm ms^{-1}$ (300 mph) of some large wind turbines, $60~\rm ms^{-1}$ (134 mph) is more relatable to the current wind turbines in operation and encompasses the average tip speeds of most wind farms. Taking this as the maximum test velocity, the distance to be travelled by each sample was then calculated by running the rig at $60~\rm ms^{-1}$ for maximum time, before the temperature conditions within the chamber varied from initial conditions. This resulted in a runtime of $60~\rm min$ and a corresponding distance of $216~\rm km$ travelled by the sample. This resulted in the $40~\rm ms^{-1}$ test having a 90-min duration each cycle, the $50~\rm ms^{-1}$ test having a 72-min duration each cycle and the $60~\rm ms^{-1}$ test having a 60-min duration each cycle.

2.5. Mass Measurement

The primary method for recording erosion after cycles was by measuring the mass loss of each sample using an *BM*-252 (*AND*) balance, measuring accurate to 0.01 mg. This allowed for direct comparison between each stage of testing and provided data detailing the impact angles and speeds most vulnerable to erosion for the G10 Epoxy Glass Fibre material [10]. Before testing, each sample had its mass measured five times, resulting in an averaged initial mass. This process was then repeated for each sample after testing and the drying period, giving a percentage error of 0.016%. The drying period consisted of the samples all under the same ambient conditions for the same amount of time to ensure accurate comparisons.

Four wear-wastage maps were then created using mass loss data after each consecutive cycle. They indicated the accumulated mass loss after each cycle with boundaries of 0.05 mg difference. Each intersection between the tick marks of velocity and impact angle indicates a sample's data point on the maps, with contour lines generated by interpolation with the *contourf* function within *MATLAB*.

Lubricants 2021, 9, 60 6 of 12

To allow for analysis of continued gradual wear after each test cycle for each individual sample and for direct comparison, mass loss data were also collated into a line graph. This allowed for direct comparison of an individual sample mass loss after each cycle, as well as compared to other samples. It also detailed the accumulated mass loss at each total distance travelled, after each respective cycle. The data are presented in these two forms as they provide the most information and visualization into the progression of erosion and an insight to mechanisms acting on the material.

To validate the mass loss measurements, an SEM study was conducted on various samples at the end of the fourth cycle to visually inspect the damage. As the samples were GFRP and non-conductive, a gold plating was applied to allow use of the SEM. The voltage was kept constant at 15 kV.

3. Results and Discussion

The mass loss from each sample was recorded and is shown in the form of an erosion map, which displays the relationship between impact velocity and impact angle in terms of mass loss [10]. The four maps, Figure 4a–d, show the four cycles the samples were exposed to and the combinations of linear impact velocity and impact angle which result in the most erosion.

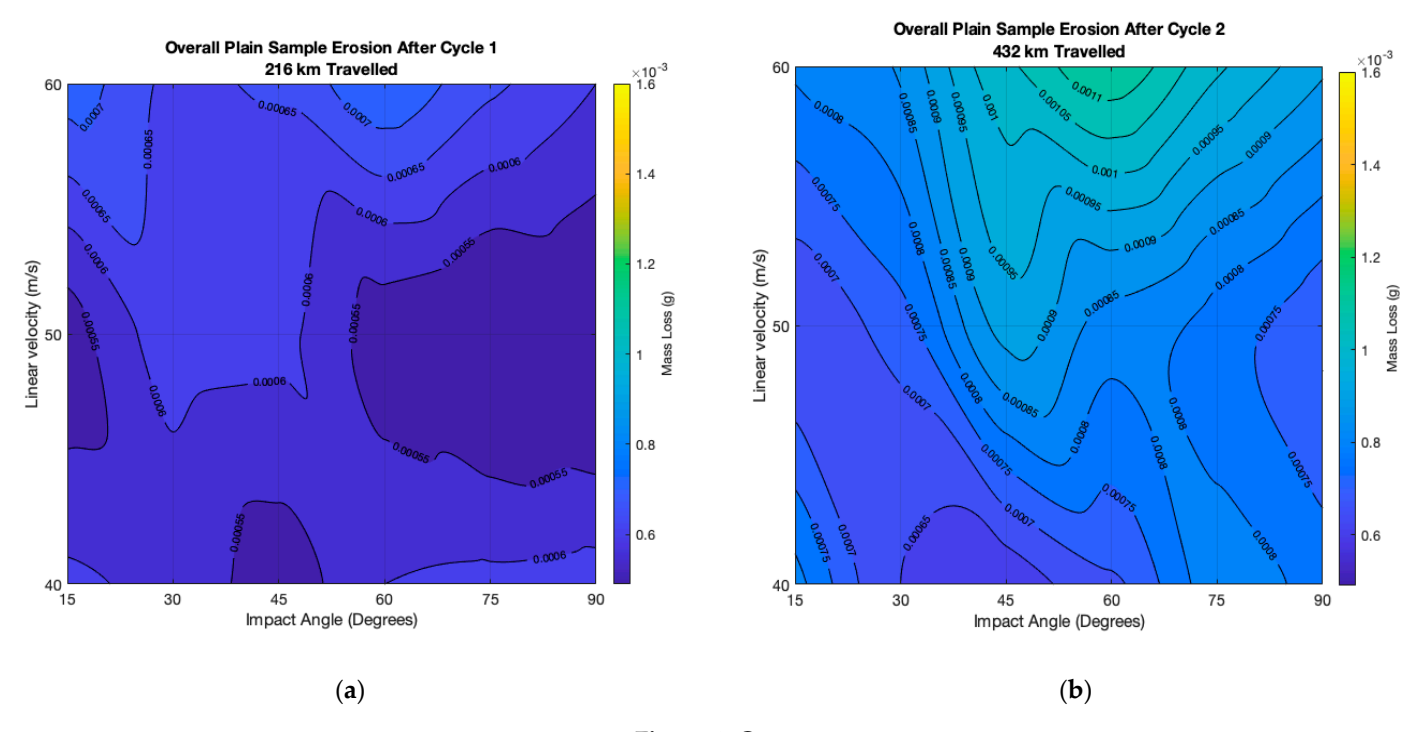


Figure 4. Cont.

Lubricants **2021**, 9, 60 7 of 12

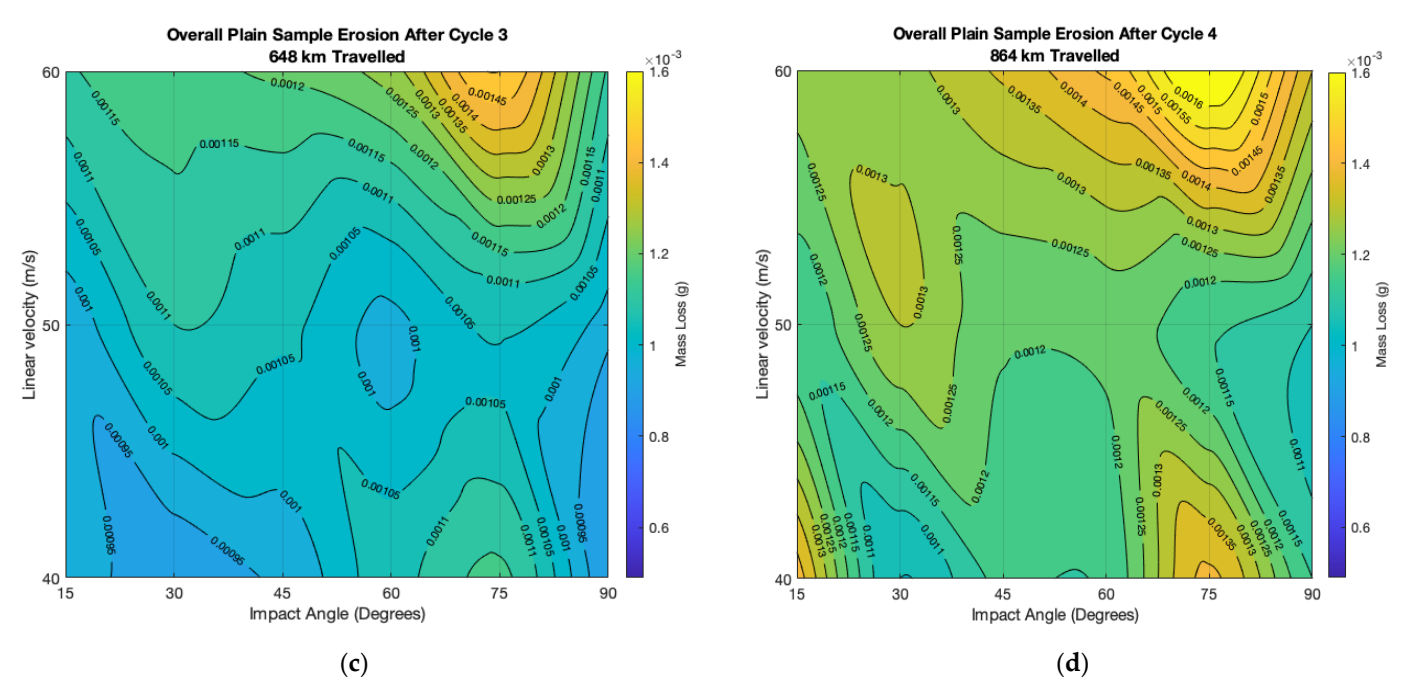


Figure 4. Mass loss results from (a) Plain Samples Mass Loss Post Cycle 1. The highest mass loss occurred at 60° at 60 ms^{-1} with a loss of 0.74 mg. The lowest mass loss occurred at 90° at 50 ms^{-1} with a loss of (0.49 mg). (b) Plain Samples Mass Loss Post Cycle 2. The highest mass loss occurred at 60° at 60 ms⁻¹ with a loss of (1.14 mg). The lowest mass loss occurred at 45° at 40 ms⁻¹ with a loss of (0.61 mg). (c) Plain Samples Mass Loss Post Cycle 3. The highest mass loss occurred at 75° at 60 ms^{-1} with a loss of (1.50 mg). The lowest mass loss occurred at 30° at 40 ms^{-1} with a loss of (0.91 mg). (d) Plain Samples Mass Loss Post Cycle 4. The sample with the highest mass loss after full testing occurred at an impact angle of 75° at a speed of 60 ms^{-1} with a loss of (1.67 mg). The lowest mass loss occurred at 30° and 40 ms^{-1} with a loss of (1.05 mg). The wear maps in Figure 4 are set up displaying mass loss and each colour in the wear map represents a range of 0.05 mg. The wear map can be used in a similar fashion to an isobar map where the spacing between the lines represents the differential in erosion. The first wear map, (a), displays the mass loss from the samples as they undergo their first cycle of 216 km equivalent exposure time. It is within this cycle the largest increase in mass loss is observed; however, the large spacing between the contour lines means that there are no specific conditions where there are large deviations in erosion. In (b), the wear map displays the mass loss for the second cycle the samples were exposed to now equivalent to 432 km in experimental distance travelled. This map displays another large increase in erosion from the previous cycle and also some concentrated areas in which there was considerably more mass loss, which includes $50~\mathrm{ms}^{-1}$ at 45° and $60~\mathrm{ms}^{-1}$ at 60°. These two samples show a large difference from the surrounding samples illustrated by the tightly packed erosion lines. The impact angles at which these samples were subject to result in the most significant degradation observed within this experiment.

Figure 4c shows the wear map following the third cycle exposure time, which is now equivalent to 648 km travelled. This wear map still displays an increase in erosion for most samples; however, the rate of mass loss has decelerated and the difference between cycles 2 and 3 is considerably less than the difference between cycle 1 to 2. The general distribution between all the samples is more neutralized within this cycle as the range in mass loss between the least and most eroded sample is lower than it is in cycle 2. This can be visualized on the wear map as the spacing between the erosion lines is greater.

Figure 4d shows the wear map for the fourth and final cycle the samples were exposed to, totalling 648 km. The trends this wear map displays are very similar to the third cycle as the mass loss of the samples continues to increase; however, the range between the samples decreases. This is also illustrated as the erosion contours grow even further apart.

Lubricants 2021, 9, 60 8 of 12

Based on the literature [16], the two main forms of erosion that the sample will encounter during testing are so-called ductile erosion and brittle fracture, as seen in Figure 5a,b. Although these figures show morphologies indicating particle impacts, similar features were observed for high velocity water impacts, as seen in the recorded Figure 5. More ductile materials have a higher erosion response at low angles of impact such as 15–30°, depending on conditions [17]. This results in plastic deformation and gouging. Consistent with the literature [16] (although this depends on the conditions), materials that are intrinsically more brittle in behaviour have a higher erosion response at higher angles of impact, such as 75–90°. This will potentially result in a fracture, crack or delamination. In this case, the G10 glass epoxy material showed peak erosion at 45–60 degrees, which is a crossover between these two characterizations. This showed evidence of both the ductile and brittle material degradation mechanisms, visually inspected from the micrographs in Figure 5. Hence, these mechanisms are the initial stages of erosion, which create initiation sites which are possibly more vulnerable to further erosion, due to the increased surface roughness. These sites are normally small pinholes in the material and are broken down quickly by lateral jetting [18], exploiting, exploiting pinholes to form cracks and removing material from the sample.

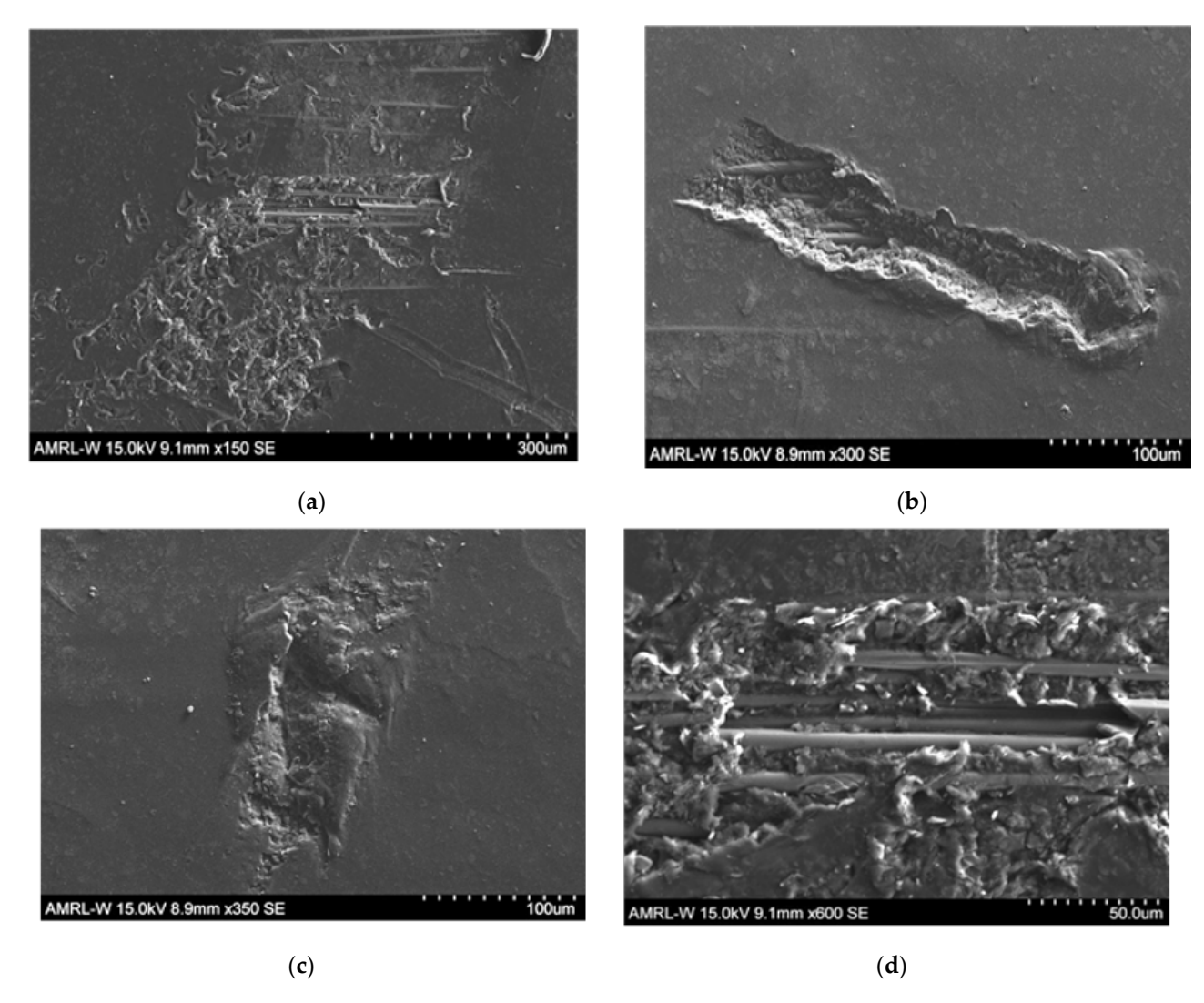


Figure 5. SEM images of erosion damage from droplet impact at: (a) $15^{\circ} \times 150 \text{ Mag}$ (b) $60^{\circ} \times 300 \text{ Mag}$ (c) $75^{\circ} \times 350 \text{ Mag}$ (d) $15^{\circ} \times 600 \text{ Mag}$.

Lubricants **2021**, 9, 60 9 of 12

Erosion mechanisms are determined by the material being subjected to these conditions, such as in this investigation where a composite material is eroded [19]. In the wind turbine industry, composites are used due to their combined properties of strength, from the glass fibres, and increased strain resistance under deformation, from the epoxy resin matrix. Glass fibres are very susceptible to brittle fracture when subject to high velocity impact, and are likely to be broken and removed, especially at high angle impacts. The epoxy resin matrix protects the glass fibres from this damage, having high elasticity and resistance to high impact angle brittle fracture. However, it is at risk from low angle of impact, and ductile erosion. Therefore, when the top surface of the composite is compromised, and pinholes emerge from the material, it is possible that the fibres are exposed and become unprotected from high velocity water droplet impacts. This trade-off can be expressed by the commonly known wear rate impingement angle line graph, as shown in Figure 6 [18], which indicates why there was an initial spike in cycle 2 at 60 ms^{-1} at 60° and at 50 ms⁻¹ at 45°. At these conditions, the water droplet compromises the elastic epoxy layer with ductile abrasion, further exploiting the hard glass fibres with brittle fracture and lateral jetting which optimizes mass removal.

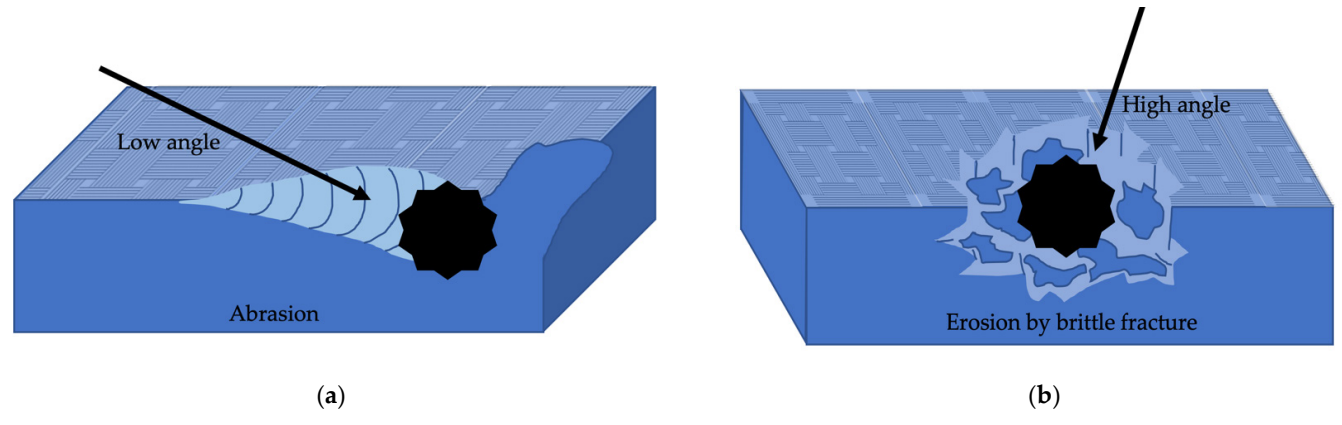


Figure 6. Wear mechanisms for particle impacts with (a) low angle of impact (b) high angle of impact. Adapted from [18].

After the 4 cycles were complete, a SEM analysis was carried out on the samples, seen in Figure 5. From these images, the following can be observed: (a) pinholes in the material and some exposed fibres, (b) a classical example of ductile erosion or abrasion, (c) a close view of a pinhole that would be extremely unprotected from lateral jetting and the cavity would be deepened and fractured, (d) an up-close view of exposed fibres, assumed to be uncovered after abrasion of the top epoxy layer. Mass loss data used to create the wear maps were also formatted to display the wear rate of the samples over the three impact velocities, as seen in Figure 7 [20]. This was completed in order to visualize the rate of mass loss between each cycle and also to compare trends with each sample. From all three line-graphs—40 ms⁻¹, 50 ms⁻¹, 60 ms⁻¹—it is clear the general trend is that for the conditions studied, most of the erosion occurred in cycles 1 and 2. At 40 ms⁻¹ and 50 ms⁻¹, the general trends in mass loss are relatively similar at lower impact angles; it is assumed that this may be due to the composite material absorbing impacts rather than fracturing in these conditions than at higher impact angles. Until cycle 2, the wear rate is approximately linear, after which the mass loss starts to reduce. This trend can also be found in the literature [21–23] and shown in Figure 8, where the erosion of a material is set into three distinct sections: incubation period, steady weight loss rate and final erosion region. From this investigation, it is assumed that the incubation period occurred during the first cycle, as there was instantly mass loss that continued linearly into cycle 2, and cycles 3 and 4 are described by the final erosion region. It is clear that are three transition points on this curve which may be linked to an erosion mechanism from deformation of the matrix material to fracture of the reinforcement material. Further, it is likely that the G10 Epoxy Glass samples used in this investigation must have had some initial surface

Lubricants 2021, 9, 60 10 of 12

roughness in order to initiate top layer erosion, shortening the incubation period. Further work will set to establish an erosion raindrop mechanistic map for these materials based on cycle time and the above observations.

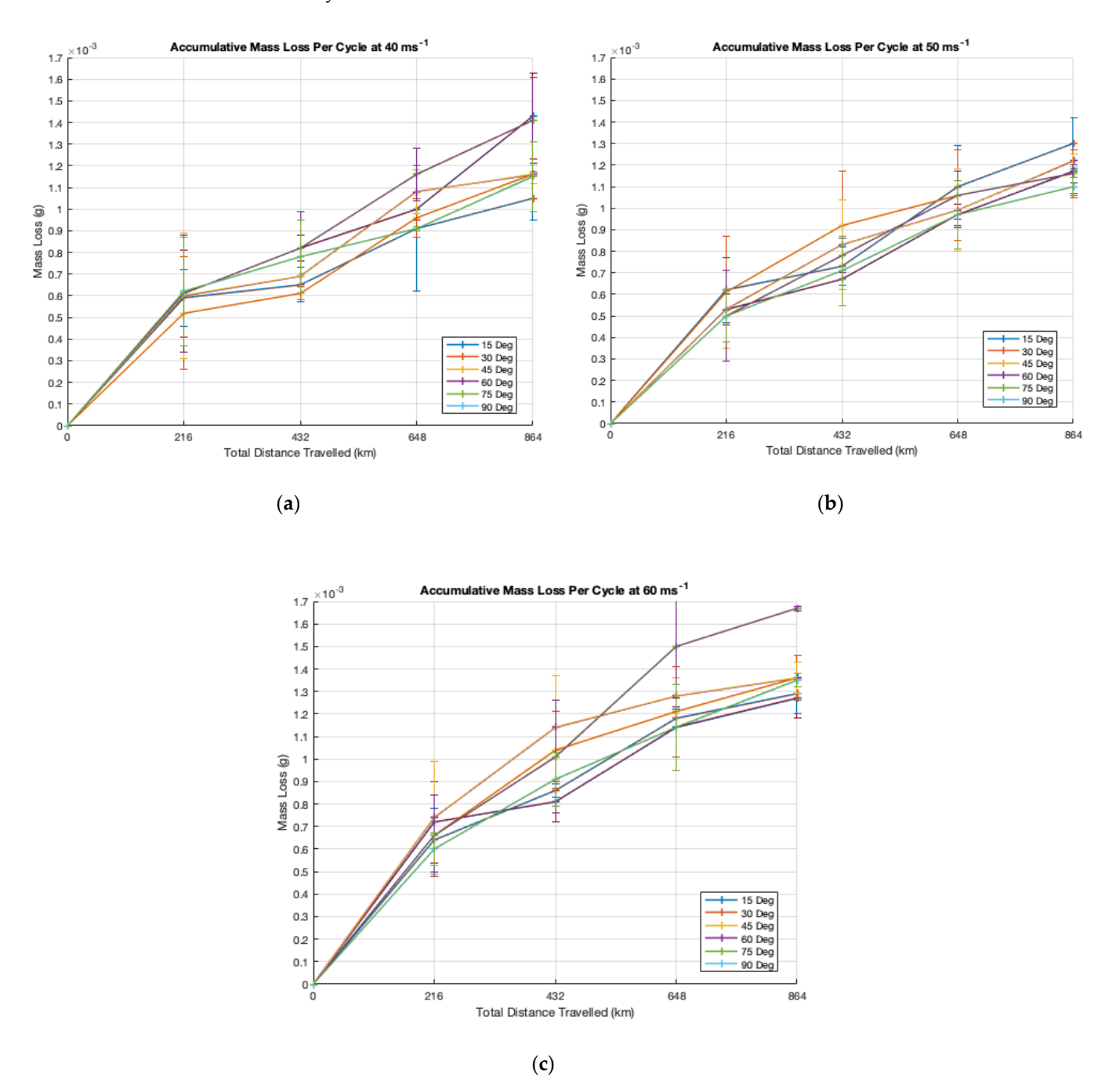


Figure 7. Accumulative mass loss for each impact velocity: (a) 40 ms^{-1} (b) 50 ms^{-1} (c) 60 ms^{-1} .

Lubricants **2021**, 9, 60 11 of 12

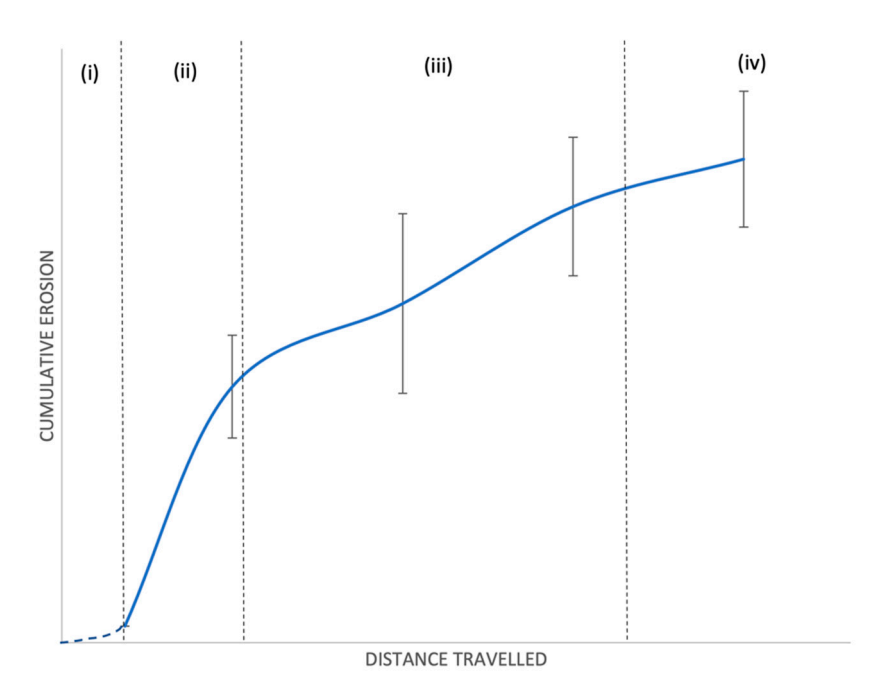


Figure 8. A schematic line graph of cumulative erosion against distance travelled created using averaged data from Figure 6 which outlines the different stages during erosion. (i) Incubation period, which was not observed during this investigation and is shown as the blue dotted line. (ii) The linear increase in erosion also known as the acceleration stage. (iii) The deceleration stage. (iv) Terminal stage.

4. Conclusions

- The wear maps as a function of impact angle and impact velocity in this study were created using the experimental results and demonstrated insights into the trends of erosion throughout the four cycles the samples were exposed to. The wear maps also allowed visualization of the magnitude of variation between samples in the same cycle, as the contours that separated each range of mass loss worked similarly to isobar lines on a pressure map. When the contours are tightly packed together, a large difference in mass loss is highlighted, and vice versa.
- The samples that experienced the most erosion were subjected to impact angles ranging between 45° and 60°. This was theorized to be due to the synergistic effects of ductile erosion or abrasion, brittle fracture and lateral jetting interacting in this impact angle range. The SEM images confirmed the existence of these wears.
- Impact angle was found to have a greater influence on erosion than the change in impact velocity between the ranges tested in this investigation.
- For the effect of exposure time, the raindrop erosion rate could be visualized over the three regimes for the conditions studied. The trend followed the same pattern as observed in the literature. Two of the three distinct erosion states were observed, with the third unrecorded erosion state being the incubation period. The material degradation followed a general trend and with more experiments and data collection, a predictive tool may be developed in order to accurately predict rain erosion on wind turbine blades.

Author Contributions: Conceptualisation, K.P. and M.M.S.; Funding acquisition, M.M.S.; Investigation, S.G. and I.Z.; Project administration, K.P.; Supervision, K.P., M.M.S.; Validation, I.Z.; Visualisation, S.G.; Writing—original draft, S.G.; Writing—review and editing, K.P., I.Z. All authors have read and agreed to the published version of the manuscript.

Lubricants **2021**, 9, 60 12 of 12

Funding: The authors would like to acknowledge the support of the Interreg (Northern Ireland—Ireland—Scotland) Special EU Programmes Grant No SPIRE2_INT-VA-049 "Storage Platform for the Integration of Renewable Energy (SPIRE 2)".

Conflicts of Interest: The authors declare no conflict of interest.

References

- 1. Roberts, D. These Huge New Wind Turbines Are a Marvel. They're Also the Future. *Vox.* 20 May 2019. Available online: https://www.vox.com/energy-and-environment/2018/3/8/17084158/wind-turbine-power-energy-blades (accessed on 6 May 2021).
- 2. Sareen, A.; Sapre, C.A.; Selig, M.S. Effects of leading edge erosion on wind turbine blade performance. *Wind. Energy* **2014**, 17, 1531–1542. [CrossRef]
- 3. International Renewable Energy Association. Future of Wind: Deployment, Investment, Technology, Grid Integration and Socio-Economic Aspects (A Global Energy Transformation paper); International Renewable Energy Agency: Abu Dhabi, United Arab Emirates, 2019.
- 4. Bartolomé, L.; Teuwen, J. Prospective challenges in the experimentation of the rain erosion on the leading edge of wind turbine blades. *Wind. Energy* **2019**, 22, 140–151. [CrossRef]
- 5. Timmer, W.A.; Schaffarczyk, A.P. The effect of roughness at high Reynolds numbers on the performance of aerofoil DU 97-W-300Mod. *Wind. Energy* **2004**, *7*, 295–307. [CrossRef]
- 6. Macdonald, J.R.; Stack, M.M. Some Thoughts on Modelling Hail Impact on Surfaces. J. Bio Tribo Corros. 2021, 7, 1–7. [CrossRef]
- 7. Zidane, I.F.; Saqr, K.M.; Swadener, G.; Ma, X.; Shehadeh, M.F. On the role of surface roughness in the aerodynamic performance and energy conversion of horizontal wind turbine blades: A review. *Int. J. Energy Res.* **2016**, *40*, 2054–2077. [CrossRef]
- 8. Siddons, C.; Macleod, C.; Yang, L.; Stack, M. An Experimental Approach to Analysing Rain Droplet Impingement on Wind Turbine Blade Materials. In Proceedings of the EWEA 2015 Annual Event, Paris, France, 17–20 November 2015.
- 9. Pugh, K.; Stack, M.M. Rain erosion maps for wind turbines based on geographical locations: A case study in Ireland and Britain. *J. Bio Tribo Corros.* **2021**, *7*, 1–7.
- 10. Pugh, K.; Nash, J.; Reaburn, G.; Stack, M. On analytical tools for assessing the raindrop erosion of wind turbine blades. *Renew. Sustain. Energy Rev.* **2021**, *137*, 110611. [CrossRef]
- 11. Elhadi Ibrahim, M.; Medraj, M. Water droplet erosion of wind turbine blades: Mechanics, testing, modeling and future perspectives. *Materials* **2020**, *13*, 157. [CrossRef] [PubMed]
- 12. DNVGL. DNVGL-RP-0171: Testing of Rotor Blade Erosion Protection Systems; Recommended Practice. 2018. Available online: https://rules.dnv.com/docs/pdf/DNV/RP/2018-02/DNVGL-RP-0171.pdf (accessed on 6 May 2021).
- 13. Pugh, K.; Rasool, G.; Stack, M.M. Some Thoughts on Mapping Tribological Issues of Wind Turbine Blades Due to Effects of Onshore and Offshore Raindrop Erosion. *J. Bio Tribo Corros.* **2018**, *4*, 50. [CrossRef]
- 14. Pugh, K.; Rasool, G.; Stack, M.M. Raindrop Erosion of Composite Materials: Some Views on the Effect of Bending Stress on Erosion Mechanisms. *J. Bio Tribo Corros.* **2019**, *5*, 45. [CrossRef]
- 15. Rasool, G.; Johnstone, C.; Stack, M.M. Tribology of Tidal Turbine Blades: Impact Angle Effects on Erosion of Polymeric Coatings in Sea Water Conditions. In Proceedings of the Asian Wave and Tidal Energy Conference (AWTEC), Singapore, 24–28 October 2016.
- 16. Jana, B.; Stack, M. A note on threshold velocity criteria for modelling the solid particle erosion of WC/Co MMCs. *Wear* **2011**, 270, 439–445. [CrossRef]
- 17. Heymann, F.J. Erosion by liquids. Mach. Des. 1970, 10, 118–124.
- 18. Stachowiak, G.W.; Batchelor, A.W. Abrasive, Erosive and Cavitation Wear. Veh. Tribol. 2006, 12, 501–551. [CrossRef]
- 19. Chen, J.; Wang, J.; Ni, A. A review on rain erosion protection of wind turbine blades. *J. Coat. Technol. Res.* **2019**, *16*, 15–24. [CrossRef]
- 20. Liquid Impingement Erosion. In *Friction, Lubrication, and Wear Technology*; ASM International: America, NY, USA, 2017; Volume 18, pp. 302–312.
- 21. Hoksbergen, T.; Baran, I.; Akkerman, R. Rain droplet erosion behavior of a thermoplastic based leading edge protection system for wind turbine blades. *IOP Conf. Ser. Mater. Sci. Eng.* **2020**, 942, 012023. [CrossRef]
- 22. Springer, G.S. Erosion by Liquid Impact; Scripta Publishing Co.: Washington, DC, USA, 1976.
- 23. Tobin, E.; Young, T.; Raps, D.; Rohr, O. Comparison of liquid impingement results from whirling arm and water-jet rain erosion test facilities. *Wear* **2011**, 271, 2625–2631. [CrossRef]